

See discussions, stats, and author profiles for this publication at:
<https://www.researchgate.net/publication/44056417>

Femtosecond time-resolved zero kinetic energy photoelectron and photoionization spectroscopy studies of I₂ wavepacket dynamics

ARTICLE *in* CHEMICAL PHYSICS · JULY 1996

Impact Factor: 1.65 · DOI: 10.1016/0301-0104(95)00404-1

CITATIONS

59

READS

26

4 AUTHORS, INCLUDING:



Albert Stolow

University of Ottawa

177 PUBLICATIONS 5,265 CITATIONS

SEE PROFILE



ELSEVIER

Chemical Physics 207 (1996) 331–354

Chemical
Physics

Femtosecond time-resolved zero kinetic energy photoelectron and photoionization spectroscopy studies of I_2 wavepacket dynamics

Ingo Fischer¹, Marc J.J. Vrakking², D.M. Villeneuve, Albert Stolow^{*}

*Ultrafast Phenomena Group, Steacie Institute for Molecular Sciences, National Research Council of Canada, Ottawa, Ontario, Canada
K1A 0R6*

Received 30 August 1995

Abstract

We report the application of femtosecond zero kinetic energy (ZEKE) photoelectron spectroscopy and photoionization to the study of bound wavepacket motion in the electronic B state of iodine by a $[1 + 2]$ multiphoton process. The experimental approach is described in detail. Comparisons of ZEKE photoelectron detection with ion detection are made. The pump wavelength was fixed at 580 nm whereas the probe wavelength was tuned from 350 to 300 nm. Wavepacket motion in the B state with the fundamental vibrational period of 340 fs was observed, as well as wavepacket dephasing and rephasing. Differences in the modulation depths and Fourier transform power spectra were observed. The phase shifts (time offset from $\Delta t = 0$) and modulation patterns varied as the location of the Condon point for the probe step changed upon tuning the probe wavelength. Higher-order wavepacket fractional revivals were observed in time-windowed Fourier transform power spectra.

1. Introduction

Femtosecond pump–probe experiments are by definition double-resonance experiments and as such may reveal more information about excited molecular states than is contained in the absorption spectrum. For homogeneously broadened systems, the information content of time-domain experiments is equivalent to frequency-resolved Doppler-free dou-

ble-resonance experiments and the two are related through the Fourier transformation, the method of choice therefore being based upon convenience. For inhomogeneously broadened systems, on the other hand, the information content is inequivalent as the spectral lineshapes are not directly related to the dynamics. In a time-resolved experiment, a pump pulse prepares an excited state which subsequently undergoes dynamic motion [1]. This might be chemical reaction, such as dissociation or isomerization, or bound (e.g. vibrational) motion. The coherent motion of the prepared state can often be discussed conveniently in terms of an excited state wavepacket [2]. A probe pulse subsequently analyzes the excited state (or the products of a chemical reaction) by projecting it onto a third, final, state, i.e. the wavepacket is decomposed in the basis set of the final state. The signal is measured as a function of the delay time

^{*} Corresponding author.

¹ Deutsche Forschungsgemeinschaft postdoctoral fellow. Present address: Laboratorium für Organische Chemie der ETH Zürich, Universitätsstrasse 16, CH-8092 Zürich.

² Present address: Department of Chemistry, Laser Centre Free University Amsterdam, Physical and Theoretical Chemistry, De Boelelaan 1083, 1081 HV Amsterdam, The Netherlands.

between the two laser pulses. The time dependence of the signal, $S(\Delta t)$, can be generally described by the equation

$$S(\Delta t) = \left| \langle \phi_f(\mathbf{r}) | \boldsymbol{\mu} \cdot \mathbf{E} | \phi_{ex}(\mathbf{r}, \Delta t) \rangle \right|^2, \quad (1)$$

where $|\phi_{ex}(\Delta t)\rangle$ is the excited state of interest, $|\phi_f\rangle$ is the final state onto which the dynamics is projected, and $\boldsymbol{\mu}$ is the transition dipole moment, which is in general a function of nuclear coordinates. The different probe techniques which are implemented in time-resolved spectroscopy can be distinguished in terms of the choice of final state. The first, and still most common probe technique applied in femtosecond experiments is time-resolved electronic spectroscopy [3,4]. In such experiments, the prepared excited state is projected onto a higher-lying electronic state and the fluorescence from this final state is collected. Another technique involves measuring the excited state absorption of the probe beam [5]. Alternatively, the dynamics can be projected back onto the ground state of the neutral (stimulated emission pumping) [6] or onto the ground state of the ion by means of photoionization [7,8]. A potential advantage of these latter techniques is that the final state is often well characterized by independent methods such as high resolution spectroscopy or *ab initio* computation.

The choice of the ground state of the ion as the final state $|\phi_f\rangle$ may have several conceptual and practical advantages: (1) charged particle detection is extremely sensitive; (2) detection of the ion provides mass information; (3) ionization is always an allowed process. Any molecular state can be ionized, whereas the electronic spectroscopy relies on the existence of optically allowed transitions. (4) Rabi oscillation between bound states, which can interfere with wavepacket measurements, does not occur in ionization. (5) Further information can be obtained by analysing the photoelectron (e.g. as to its kinetic energy), analogous to dispersed fluorescence methods.

In polyatomic molecules, the wavepacket will in general evolve simultaneously along several nuclear coordinates i.e. the wavepacket is multidimensional. Motion along each coordinate can contribute to the time-dependent signal and these various components can sum in a very complicated manner. It might be

attractive to consider detection schemes which filter these various components by projecting them onto different final states, if this is possible. For example, in electronic spectroscopy either the total or dispersed fluorescence [9] can be collected. If the molecular dynamics is projected onto the various vibrational levels of the ionic ground state, detection of the total ion yield is analogous to the total fluorescence technique, whereas analysis of the photoelectron energies is analogous to a dispersed fluorescence technique. Several theoretical studies showed possible advantages of time-resolved photoelectron spectroscopy [10,11], suggesting that detailed information related to excited state dynamics might be revealed by such measurements.

ZEKE spectroscopy [12,13], relies on the excitation of molecules into high lying, long-lived Rydberg states ($n \geq 150$) converging onto a state of the ion. These Rydberg states can survive for several microseconds, depending upon conditions. In a few favourable cases lifetimes of more than 100 μs were reported [14]. The Rydberg states are field ionized by a pulsed electric field, applied after a suitable delay time (on the order of 100 ns to several μs). During the delay time, kinetic electrons leave the interaction region and are not detected. In frequency-resolved ZEKE experiments, the spectroscopy of the molecular ion is studied by monitoring the electron signal as a function of the laser wavelength. In time-resolved ZEKE experiments, a final state of the ion is chosen and the signal is monitored as a function of the pump–probe time delay, reflecting the excited state dynamics. In the picosecond domain, dynamical phenomena such as intramolecular vibrational energy redistribution (IVR) [15] and predissociation [16] have been investigated using ZEKE detection. In the femtosecond domain, ZEKE detection was applied to the Na_3 [17] system.

A potential advantage of ZEKE spectroscopy in fs pump–probe experiments is that certain higher-order processes (e.g. multiple absorption of either pump or probe photons) may produce kinetic electrons which contribute to background signals in a conventional photoelectron spectrum, but do not necessarily excite long-lived Rydberg states. This can become important because femtosecond pump–probe experiments are often high intensity experiments: a 100 fs pulse with 1 μJ of energy under mild focusing conditions

($f/40$) yields an intensity on the order of a TW/cm^2 . We have discussed elsewhere [18] the intensity effects which can occur in photoelectron spectroscopy when using femtosecond pulses. Another aspect of ZEKE spectroscopy is that symmetry selection rules are often relaxed [19], allowing for the observation of additional dynamical motion. This is because the final electron state can achieve whichever symmetry is required to induce the transition. This relaxation of selection rules was illustrated recently in frequency-domain studies of CH_3I photodissociation. In resonance Raman spectroscopy [20] only emission into totally symmetric modes of the ground state was observed. By contrast, in two-photon ZEKE spectroscopy [21], additional signals from non-totally symmetric vibrations were recorded, giving experimental evidence for the importance of the $\text{H}_3\text{-C-I}$ bending vibration in the dissociation process.

In a recent communication [22] we reported the application of ZEKE photoelectron spectroscopy as a detection technique to the study of wavepacket dynamics in the $\text{I}_2 \text{B}0_v^+$ state. This state was previously studied in detail by Zewail and co-workers using both fluorescence [23] and ionization [24] detection. They demonstrated that a highly accurate B-state potential could be constructed by inversion of the time-domain data [25]. Exact time-dependent quantum mechanical calculations were performed to analyze the influence of the coherent vibrational motion on the fluorescence spectra [26].

In our femtosecond experiments [22], we excited iodine to the B state with one photon around 580 nm, coherently populating vibrational levels around $v' = 15$. The dynamics of the wavepacket motion was then probed by means of a two-photon excitation, with detection of either ZEKE photoelectrons or ions. In Fig. 1 we show a simple depiction of the potential energy curves of the iodine molecule that are of interest in the present experiment. The initial state X is the neutral ground state, the $\text{B}0_v^+$ is the excited state we are studying and the ionic ground state X^+ is the final state onto which we project the dynamics. The curves represent fits to Morse potentials which were used in wavepacket calculations, discussed below. The probe wavelength was varied from around 350 (just below the ionization threshold) to around 300 nm. In the case of iodine, a wavelength shorter than 175 nm would be required

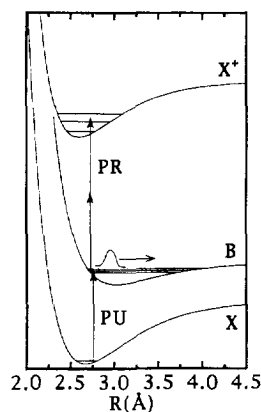


Fig. 1. Illustrative potential energy curves of I_2 . All curves are fitted Morse potentials. A B-state wavepacket is prepared by 580 nm excitation into the B state. The wavepacket dynamics is probed as a function of the pump–probe delay time via two-photon ionization into the ground state of the ion. Electrons, high- n Rydberg states or ions may be detected.

in order to probe the B-state dynamics with a single photon. Although there is considerable effort devoted to the production of femtosecond vacuum ultraviolet (VUV) radiation [27,28], we chose for reasons of experimental simplicity a two-photon detection scheme in the present experiments. By tuning the probe laser we examined the effect of changing the final state on the form of the ZEKE and ion time delay scans.

In this paper, a detailed comparison of ion with ZEKE detection of wavepacket dynamics as a function of probe laser wavelength is presented and methods for analysing the frequency content of time delay scans and their phase shifts (offset) from zero time delay are discussed. The experimental approach is described in considerable detail. The dynamics of the B state of iodine is discussed in terms of wavepacket motion and the detection of wavepacket dynamics is analyzed in terms of Franck–Condon factors for the probe step. Fourier transform power spectra (hereafter called FTs) of the time delay scans revealed that the frequency content of these scans can be assigned to level spacings in the molecular B state, as expected. Differences between ZEKE and ion scans can be seen in the modulation depths and the FTs of the scans. In the subsequent section, ZEKE and ion time delay scans for different probe

wavelengths are presented, showing the effects of varying the final state. The determination of the absolute pump–probe $\Delta t = 0$ is discussed and the phase shifts as a function of probe wavelength are presented. Time-windowed FTs (spectrograms) of the data are used in order to determine the frequency content of the scans as a function of delay, revealing evidence for higher-order fractional revivals (i.e. higher-order rephasings of the wavepacket). Intensity effects due to the probe laser are discussed in the last section.

2. Experimental

2.1. Summary

Mode-locked Ti:sapphire (Ti:Sa) lasers provide researchers with a convenient, tunable femtosecond laser oscillator. However, for some gas phase chemistry experiments with pulsed molecular beams, microjoule pulse energies at lower repetition rates are desirable, requiring amplification. In our experiments, a phase-lock synchronized amplified picosecond Nd:YAG laser [29], discussed below, is used as the pump source for this amplification. For the ZEKE technique, it is important to be able to choose different final states in an experiment. Very broad tunability is required and was achieved by generating a white light continuum [30] and reamplifying the desired colour. A molecular beam photoelectron/photoion spectrometer was used to produce a pulsed supersonic beam of iodine, seeded in helium. The femtosecond pump and probe lasers intersected the beam at the interaction point of the spectrometer and both ion and ZEKE photoelectron signals were recorded as a function of time delay.

2.2. Detailed description

2.2.1. Amplified femtosecond laser system

The laser system, shown schematically in Fig. 2, implements two phase-locked loops (PLL) to synchronize two laser oscillators with the zero crossings of an external 80 MHz reference source. The fs oscillator used in these experiments is a regeneratively mode-locked Ti:Sa femtosecond laser [31] (Spectra Physics Lok-to-Clok Tsunami) which uses

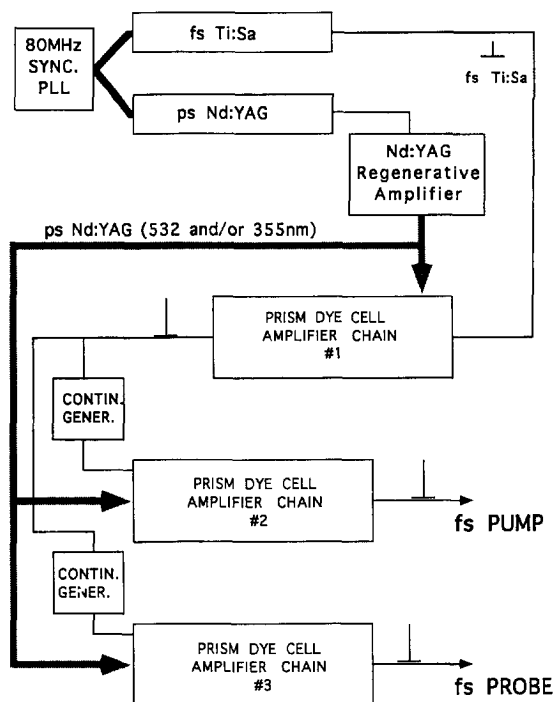


Fig. 2. Schematic of the laser system. A femtosecond Ti:Sa laser and a ps Nd:YAG laser are synchronized by phase-locking to an external 80 MHz reference. The ps Nd:YAG laser is regeneratively amplified at 20 Hz in order to pump three prism dye cell amplifier chains. Continuum is generated and a selected part of it amplified, thus providing independently tunable fs pump and probe pulses.

the first PLL [32]. The second oscillator is a diode pumped picosecond Nd:YAG laser (Lightwave Electronics 131), using the second PLL. Both oscillators are locked to the same 80 MHz reference and are therefore synchronized. Optical cross-correlation measurements confirm that the phase noise between the two lasers is less than 1–2 ps, a small fraction of the Nd:YAG pulse duration. The ps Nd:YAG pulses were subsequently amplified to 30–50 mJ/pulse at 20 Hz in a diffraction filtered unstable resonator regenerative amplifier (Positive Light RGN-A). They subsequently passed through a 9 mm power amplifier to yield 200–250 mJ/pulse. An etalon was installed in the ps Nd:YAG laser cavity in order to increase the pulse duration from 25 to 150 ps. The reasons for this are: (1) with longer ps pulses, amplification in the regenerative amplifier is gain- rather than damage-limited; (2) the longer ps pulse duration

matches the gain storage time of typical dyes under our pumping conditions; (3) longer pulses permit transverse pumping of prism dye cells, giving both alignment insensitivity and a spatial decoupling of the pump mode from the seed mode, allowing for simple, near diffraction-limited amplification of femtosecond pulses [33]. The output of the regenerative amplifier can be frequency doubled and tripled, yielding up to 100 mJ at 532 nm and 40 mJ at 355 nm. For the present experiments, we used the 532 nm pulses to transversely pump three, three-stage image-relayed prism dye cell amplifier chains, the first to amplify the output of the Ti:Sa laser, the other two to amplify white light continua for pump and probe pulse production. Pumping with synchronized transform-limited ps pulses, we find that typical shot-to-shot energy fluctuations in the amplified fs pulse are between 5–10%. The efficiency of the amplification is greatly increased due to the good temporal overlap between the ps pump and the fs seed pulse. The relatively low energy of the ps pulses allows the use of inefficient and/or short-lived dyes. We find that no saturable absorbers are required as the ASE output of the amplifier chains can be adjusted to be very small (1% by energy) [34,35]. In cases where the output pulse was frequency doubled or tripled for an experiment, higher ASE was permitted (10–30%).

The first dye amplifier chain, depicted in Fig. 3 (top), is operated with LDS 765 dye. The fs pulses from the Ti:Sa laser were amplified to 150–200 μ J pulse energy. The dye cells in this chain were deliberately underfilled, ensuring a near diffraction-limited output. The shot-to-shot energy fluctuations were less than 7%. The pulse was recompressed to about 80 fs in a grating compressor.

2.2.2. Continuum generation

For this experiment, two independently tunable fs pulses were derived from the amplified Ti:Sa pulse by generating a white light continuum and then amplifying a selected bandwidth in another dye amplifier, as depicted in Fig. 3 (bottom). General problems associated with continuum generation are: (1) the filamentary structure developed at the input beam focus, which destroys the spatial structure of the beam and (2) the shot-to-shot fluctuations in the pulse spectrum. Both of these effects impair the

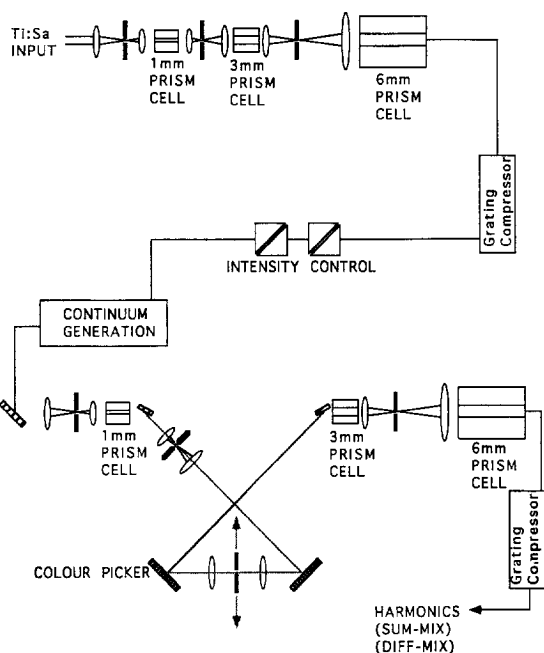


Fig. 3. The fs Ti:Sa pulse is amplified in the first prism dye cell chain. Crossed polarizers are used to control the intensity in the region of threshold continuum generation. The continuum is passed through the first dye cell of a subsequent dye chain, spatially filtered and selected in a colour-picker: by adjusting the width and position of a slit, the central wavelength and bandwidth of the pulse are selected.

recompressibility of the pulse and they can be greatly reduced by working at the intensity threshold for continuum generation [36,37]. The output of the Ti:Sa amplifier was split into two parts and each was passed through two crossed Glan–Taylor polarizers: by adjusting the relative angle between the two polarizers, the pulse energy was accurately adjusted to the threshold energy.

In all laser amplifiers, the seed pulse power competes with the noise-equivalent power of the spontaneous fluorescence (which upon amplification becomes the ASE) [38]. As the energy per unit bandwidth in the white light formed by threshold continuum generation is on the same order as the noise-equivalent input, the ASE competes efficiently with the seed pulse. In order to avoid this problem, we installed a “colour-picker” between the first and second dye cells, passing the entire continuum through the first dye cell, as shown in Fig. 3 (bottom). The first two cells were thus both spectrally

and spatially decoupled. As the seed pulse entering the second dye cell was considerably more intense than its noise-equivalent input, competition with ASE was no longer a problem. The amplified continuum pulse was compressed in a grating compressor.

The colour-picker, which selected the central wavelength and bandwidth, operates in the following way. The amplified white light continuum from the first dye cell was dispersed on a grating and focused onto a slit assembly. The wavelength was selected and varied over the gain profile of the dye by translating a slit along the focal plane of the laser pulse. The lens and grating on the output side of the slit reconstructed the pulse both spatially and spectrally. One advantage of the colour-picker is the ability to independently choose the bandwidth (and, hence, the pulse duration) by adjusting the width of the slit. A disadvantage is that it cuts the spectrum sharply as compared with an interference filter, lengthening pulses slightly. In more recent experiments, we have used exclusively interference filters. The central wavelength and bandwidth of the pulse were determined, in a single-shot manner, by sending an attenuated pulse via an optical fiber to a 0.2 m monochromator (0.1 nm resolution) where it was dispersed onto a linear diode array (EG&G Reticon). The input intensity for the continuum generation was adjusted for stability by monitoring the single-shot spectrum of the amplified continuum.

2.2.3. Iodine experiments

In the present experiment we operated one dye chain with rhodamine 610, which provided a pump energy of up to 120 μJ after recompression, centred around 580 nm with a bandwidth of 6.5 nm and pulse duration of about 95 fs, assuming Gaussian pulse shape, as shown in Fig. 4. The bandwidth product $P = \Delta\tau\Delta\nu$, was 0.54, compared to the 0.441 limit for a Gaussian pulse. This pulse served to excite iodine into the electronic B state. The other dye chain provided the probe pulse and was operated with different dyes in order to cover a wavelength range from 600 to 700 nm. The exact pulse duration and bandwidth depended on the chosen wavelength, but the bandwidth product was similar to that of the pump chain. The output was frequency doubled in a 0.1 mm BBO crystal, yielding up to 30 μJ UV light (300–350 nm) of approximately 100 fs duration.

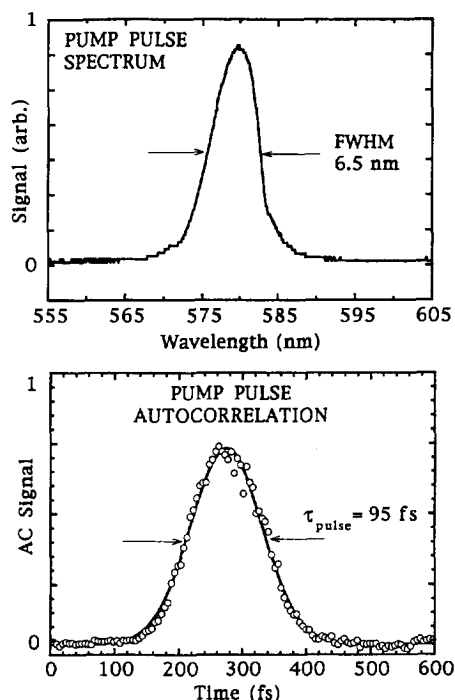


Fig. 4. Pulse characteristics of the amplified continuum pump pulse. Top: spectrum of the pulse, centered around 580 nm with a bandwidth of 6.5 nm. Bottom: non-collinear autocorrelation of the 580 nm pulse. Experimental data points are given by full circles, a Gaussian fit to the autocorrelation trace (full line) indicates a pulse duration of 95 fs full width at half maximum (FWHM).

The pump beam was retroreflected using a computer controlled motorized delay stage (Newport-Klinger) in order to control the relative timing of the two pulses. The beams were combined on a dichroic beamsplitter and focused into the molecular beam photoelectron spectrometer (discussed below) with a 400 mm quartz lens. The distance of the lens from the interaction region was chosen so that the probe pulse (energies of 5–10 μJ /pulse in these experiments) was focused close to the molecular beam axis (estimated spot size 100 μm). The pump pulse (energies of 1–30 μJ /pulse in these experiments) had a spot size of about 1 mm. We estimate that the intensity of the probe beam in the interaction region was on the order of 10^{12} W/cm² and that of the pump beam about two orders of magnitude smaller. Both pump and probe pulse energies were recorded on a shot-to-shot basis using integrating sphere/photodiode detectors. The polarization of pump and

probe beams were parallel in these experiments, although experiments with perpendicular polarization were also performed.

2.2.4. Molecular beam ZEKE photoelectron spectrometer

The second component of the experiment is an ultrahigh vacuum molecular beam photoelectron/photoion spectrometer, shown schematically in Fig. 5. It consisted of a source chamber, pumped by a 2000 l/s diffusion pump (Edwards Diffstak) and a UHV main chamber, housing two coaxial time-of-flight (TOF) spectrometers, one for electron and one for ion detection. Each TOF spectrometer was differentially pumped by a 400 l/s turbo pump (Seiko Seiki STP400). A 400 l/s corrosion resistant turbo pump (Seiko Seiki STP400C) pumped the main chamber. A mixture of 0.04% iodine in 1000 Torr He was expanded at room temperature through a piezoelectrically driven pulsed supersonic valve [39], labelled (a), with a 1 mm orifice diameter. About 20 mm downstream of the nozzle, the beam passed into the main chamber through a 1 mm diameter skimmer (Beam Dynamics), labelled (b). The base pressure in the main chamber and time-of-flight spectrometers was on the order of 10^{-10} Torr. Optical baffles (not shown) along the laser axis (marked by x) reduced scattered light to very low levels.

The molybdenum charged particle optics are also shown in Fig. 5. Two apertures with meshes, labelled (1) and (3), are separated by 20 mm and form the extraction region. In the ZEKE detection mode, an extraction voltage pulse $-V$ (typically between -2 and -32 V, after a 0.1 – 1 μ s delay) was applied to the electrode (1). Two guard rings (2), added to improve the homogeneity of the extraction field, were at potentials of $-1/3$ and $-2/3$ V during this pulse while the electrode (3) was held at ground potential. Pulsed postacceleration (4) and Einzel lens elements (5) are shown. After a flight length of about 220 mm, the electrons were detected in a dual stage microchannel plate assembly (6). The electron spectrometer sits inside a thick-walled μ -metal tube (7) which reduced the earth's axial magnetic field experienced by the electrons by a factor of 500 and the radial magnetic field by a factor of 1000, as measured at the interaction point by a Bartington Instruments fluxgate nanoteslameter.

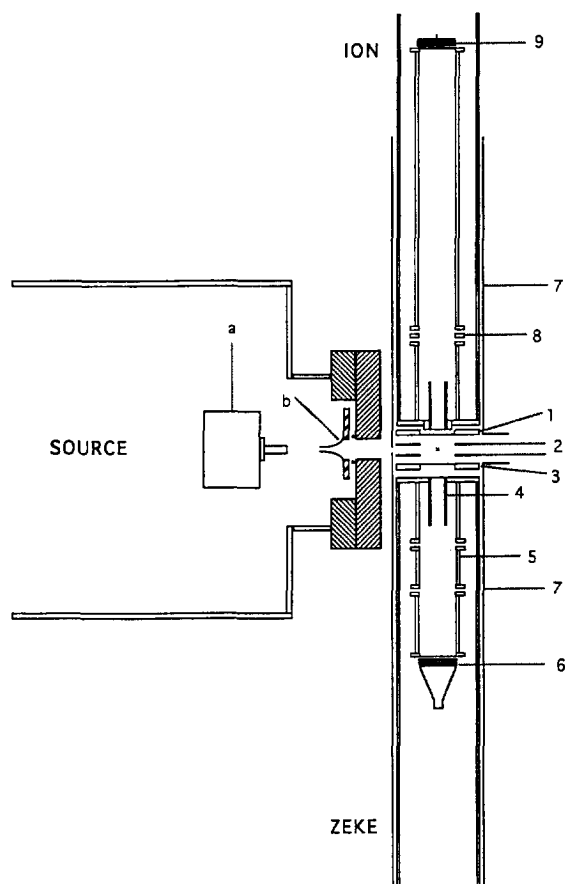


Fig. 5. Schematic of the molecular beam photoelectron spectrometer, consisting of a source chamber, a main chamber and two coaxial flight tubes. The source chamber houses a pulsed valve (a) and a skimmer (b), moveable on a gate valve which separates the source and main chambers. The interaction region consists of charged particle optic elements and is confined by the apertures (1) and (3). Two guard rings (2) are added to improve field homogeneity. Further elements include electron postacceleration (4), Einzel lenses for electrons (5) and ions (8) and microchannel plate detectors for electrons (6) and ions (9). The photoelectron spectrometer is housed inside a μ -metal tube (7), reducing external magnetic fields.

The photoion spectrometer follows the Wiley–McLaren design [40]. In the ion experiments, a high pulsed or dc voltage (typically $+500$ V) was applied to electrode (3), while (1) is kept at ground. The Einzel lens (8) could enhance the collection efficiency. The flight length was about 500 mm. The ion drift tube itself was floated at -2000 V. Another

dual stage microchannel plate assembly served as the ion detector (9).

3. Results and discussion

3.1. Wavepacket dynamics

We consider now the dynamics of $I_2(B)$ observed using time-domain techniques. We shall use the ground state of the ion as the final state and compare photoelectron with photoion detection. There are three aspects to a femtosecond pump–probe experiment: the preparation, the evolution and the probing. The pump pulse coherently excites a superposition of excited state vibrational levels a wavepacket. The amplitudes and initial phases of these prepared states are determined by the pump laser and the transition probabilities. Once the pump laser pulse is over the wavepacket, given by Eq. (2), evolves freely according to relative energy phase factors in the superposition:

$$|\chi(\Delta t)\rangle = \sum_n a_n |v_n\rangle e^{-i2\pi c E_n(v_n)\Delta t}. \quad (2)$$

The a_n coefficients contain both the amplitudes and initial phases of the vibrational states $|v_n\rangle$ which are prepared by the pump laser. The E_n are the excited state vibrational term values in wavenumbers. We note that the initial phases of the prepared states may be affected [41] by the non-zero pump pulse duration – requiring a proper treatment of the turn-on and turn-off of the pulse – and by saturation effects.

The probe laser pulse interacts with the wavepacket after the pump pulse is over, at some time delay Δt . The final detection step (e.g. collection of electrons) is incoherent because the measured signal is a sum of the ion state *populations* and, hence, there are no interferences between ionic states. Therefore, the time dependence of the signal $S(\Delta t)$ can be visualized in terms the following equations for a vibrational wavepacket.

$$S(\Delta t) = \left| \langle \Psi_{\text{ion}} | \boldsymbol{\mu} \cdot \mathbf{E} | \chi(\Delta t) \rangle \right|^2 \\ = \left| \sum_n b_n e^{-i2\pi c E_n \Delta t} \right|^2,$$

where

$$b_n = a_n \langle \Psi_{\text{ion}} | \boldsymbol{\mu} \cdot \mathbf{E} | v_n \rangle, \\ S(\Delta t) = \sum_n \sum_m b_n b_m \cos[(E_n - E_m)2\pi c \Delta t]. \quad (3)$$

The b_n coefficients contain the a_n as well as the transition dipole moment and Franck–Condon factors to the final state. The measured signal, $S(\Delta t)$ is related to the overlap of the coherent sum of prepared states with a given final state of the ion and is modulated as a function of time, as can be seen from Eq. (3). The modulations are due to interferences between the individual transitions from different eigenstates terminating in the same final ionic state and are described by nearest-neighbour coherences (i.e. when $n = m \pm 1$) as well as higher-order coherences (e.g. next-nearest-neighbour, $n = m \pm 2$). In the time-domain picture, the modulation reflects the wavepacket motion in the excited state. The wavepacket can only be detected in the region where the overlap with the final state is good. Therefore as the wavepacket oscillates, it periodically passes this region, leading to a modulated signal.

We show typical pump–probe delay scans using ion and ZEKE detection in Fig. 6. For a pump pulse around 580 nm, we prepare a set of vibration levels around $v' = 15$. The level spacing around $v' = 15$ leads to modulations with a period of 340 fs (i.e. the average classical vibrational period of $I_2(B)$ around $v' = 15$ is 340 fs). However, the level spacings vary due to the anharmonicity of the B-state potential and, as time goes on, the 340 fs modulations disappear as the vibrational states get out of phase with each other. The phase relationships between the states remain well defined, nonetheless, as the molecule neither radiates nor collides on this time scale. Therefore the states rephase, giving rise to a recurrence near 18 ps called the half-revival where the 340 fs modulation is seen again: this appears at a well defined time (related to the anharmonicity) and corresponds to a reconstructed [42] wavepacket.

Anharmonic oscillator energy levels $E_n(\omega, \alpha)$ are described by $E_n = \hbar \omega (n - \alpha n^2)$. For a coherent superposition of the E_n , the full revival time [42] is $T_{\text{rev}} = 2\pi/\omega\alpha$ at which point the phase differences (modulo 2π) between the E_n is independent of n . Hence, near this time the original wavepacket is

reconstructed. At times $t/T_{\text{rev}} = p/q$ (where p/q is an irreducible fraction of integers), the phases within subsets of eigenfunctions E_n coincide and for some values of p/q , the wavepacket splits into sets of sub-wavepackets. For example, at the quarter-revival (i.e. when $p/q = 1/4$), the wavepacket splits into two equal parts exactly out of phase, leading to a doubling of the modulation frequency in the time delay scan. Quarter-revivals have been observed in atomic Rydberg wavepackets [43].

In order to understand the modulation patterns in Fig. 6, it is helpful to consider the diabatic dressed state picture, shown in Fig. 7 for 345 nm probe wavelength. In this picture, the photon field is included explicitly in the molecular Hamiltonian, but

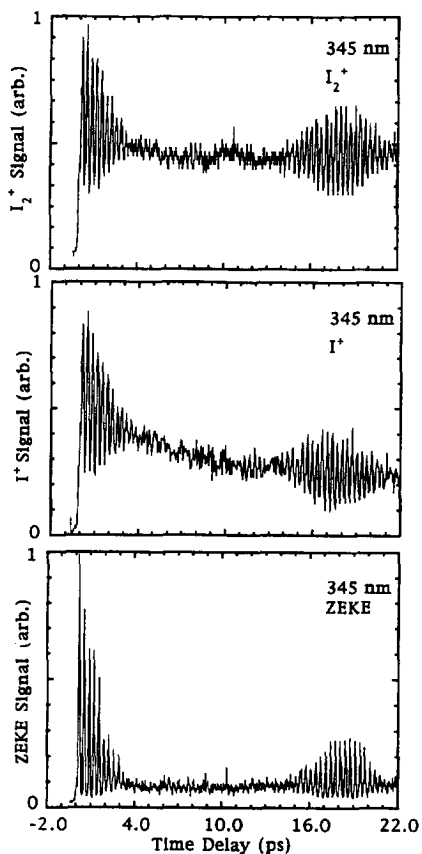


Fig. 6. Molecular ion (top), atomic ion (middle) and ZEKE (bottom) time delay scans at a probe wavelength of 345 nm, corresponding to exciting the molecule into $v^+ = 0, 1$ of the ion. The signal is modulated with a 340 fs period. The dephasing of the wavepacket and its revival (at 18 ps) is seen.

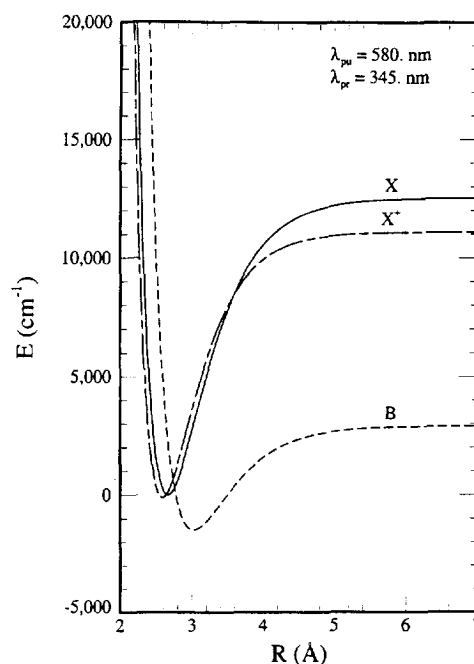


Fig. 7. Diabatic dressed states picture of I_2 photoionization at 345 nm probe wavelength. The zero in energy is defined by the ground state of the neutral, X. The B state is shifted down in energy by one pump photon, the ionic ground state, X^+ , by one pump and two probe photons. The Condon point for the X–B transition is at the intersection of the X and B curves (and likewise for the B– X^+ transition).

the Hamiltonian is not rediagonalized. We choose the ground state of the neutral (X) to define the zero on the energy scale. All other states are shifted down in energy from the values given in Fig. 1 by the photon energy with which they are accessed: the B state is shifted by one pump photon and the ionic ground state (X^+) by one pump and two probe photons. Due to conservation of energy, optical transitions cannot make a vertical change. If the dependence of the transition dipole moment on the nuclear coordinates is neglected, one can estimate the coordinate from which the classical transitions “occur” by looking for the Condon points for the pump and probe steps. The Condon point is the stationary phase point of the radial nuclear overlap integral and is the coordinate for which the kinetic energy remains unchanged during the transition [44]. It follows that in the diabatic dressed state picture, the Condon points correspond to the points of intersec-

tion of the potential energy curves. From Fig. 7, we expect the pump transition to form a wavepacket at the *inner turning point* of the B state.

The probe transition has significant probability at times when the wavepacket is localized at the probe Condon point—the intersection of the B and X^+ curves. The probe Condon point should move towards larger I–I separations when the probe wavelength, λ_{pr} , is tuned to the blue. This is because the B state is quite extended as compared with the ground states of the neutral and ion and therefore we expect Franck–Condon factors to improve for the higher vibrational levels of the ion and, furthermore, that their point of best overlap moves towards the middle of the potential. In such a case we might expect to see a doubling of the modulation frequency as the wavepacket passes the probe Condon point twice upon each vibration. This is discussed in more detail below. The relative location of the probe Condon point is related to the shift of the first signal maximum with respect to the zero in time. We hereby define this shift to be the *phase shift*. With a two-photon probe tuned close to the ionization threshold (345 nm), the probe Condon point is at (or close to) the inner turning point of the B state and we might expect close to zero phase shift for this modulation pattern, since preparation and probing can occur from almost the same geometry.

Discrete Fourier transform power spectra (FT) of the scans of Fig. 6 are shown in Fig. 8, revealing the spectral content of the time-domain data. The largest peak, centered around $\omega = 99 \text{ cm}^{-1}$, can be assigned to the level spacing between $v' = 15$ and $v' = 16$ in the B state. The other peaks are assigned to other nearest-neighbour coherences as indicated and their observation confirms that we pump and probe the vibrational levels $v' = 13$ – 18 of the B state. The spectral content of the molecular ion (top), atomic ion (middle) and ZEKE (bottom) scans are quite similar. The contributions of other electronic states of iodine to the absorption cross-section in the visible are well known [45]. About 86% of the absorption probability at 580 nm is due to the B state, 10% to the 1I_u state, and 4% to the directly dissociative $A(^3I_u)$ state. Thus, we observed almost exclusively contributions from the B state. In order to confirm that we indeed implemented a two-photon probe step, as opposed to some higher-order process, we

measured the threshold tuning curve for the probe laser, as discussed in Appendix A.

3.2. Comparison of ZEKE and ion signals

One of the most interesting differences between the ZEKE and ion scans at 345 nm (Fig. 6) is the modulation depths. They are much deeper in the ZEKE signals. We expect the ion and ZEKE scans to be similar at the ionization threshold because we prepare the same wavepacket and project it onto the same final states (since the number of open channels is small at threshold). Furthermore, it is interesting to

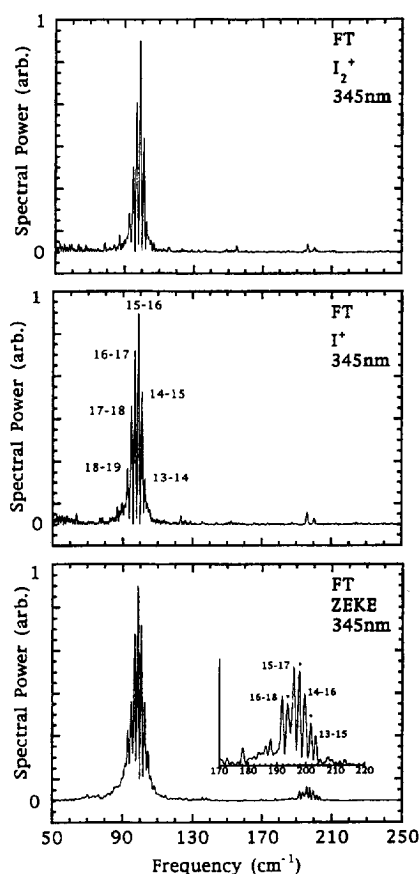


Fig. 8. Fourier transform power spectra (FT) of 25 ps time delay scans at threshold (345 nm probe) for the molecular ion (upper trace), atomic ion (middle trace) and ZEKE (lower trace) signal. The observed peaks are assignable to the level spacings of $I_2(B)$. Note the more prominent appearance of the second harmonic in the ZEKE scan (discussed in the text).

note that in the FTs shown in Fig. 8, the second harmonic contribution is very small in the ion scans, but more prominent in the ZEKE scan. In the latter there are peaks near 200 cm^{-1} , labelled by * in Fig. 8 that are *not* assignable to next-nearest-neighbour coherences and in fact do not correspond to any level spacings in the isolated molecule. They are, surprisingly, assignable to *sum-frequencies* of nearest-neighbour coherences. This result and the deeper modulation depths observed in ZEKE scans are related to unique aspects of the ZEKE detection technique itself and derive from collision-induced lifetime enhancement (i.e. ion–Rydberg interactions) of Rydberg states. The ZEKE technique relies upon preparing high- n Rydberg states which survive for long times (μs). The Rydberg states prepared by the laser, however, are low- l states which have significant overlap with the ion core (hence, a non-zero decay rate). The n states which survive for long times will also have high- l character. A mechanism for introducing high- l character is through interaction with external electric fields, which may come from surfaces or free charged particles. In the latter case, (where cylindrical asymmetry leads to non-conservation of m) we can understand the stabilization to originate from a (l,m) -changing interaction of a Rydberg state with an ion. This coupling of Rydberg state lifetime with ion concentration implies that the latter may *modulate* the Rydberg detection efficiency, leading to cross-terms in the observed ZEKE modulation frequencies and to enhanced modulation depths. This is discussed in detail in a separate publication [46].

In order to explore the influence of the final ionic state on the ion and ZEKE scans, we varied the probe wavelength between 350 and 300 nm, as shown in Fig. 9 for the I_2^+ scans. It is important to note that the ZEKE scans were very similar to the ion scans at all wavelengths. This is discussed in more detail below. The pump wavelength was fixed (580 nm) and therefore the *same* wavepacket was prepared in all experiments reported in this communication.

In principle, ion versus ZEKE detection of wavepacket dynamics can yield different results. If an ion signal is recorded, all ionic states which are energetically accessible can be populated according to their individual transition probabilities (e.g.

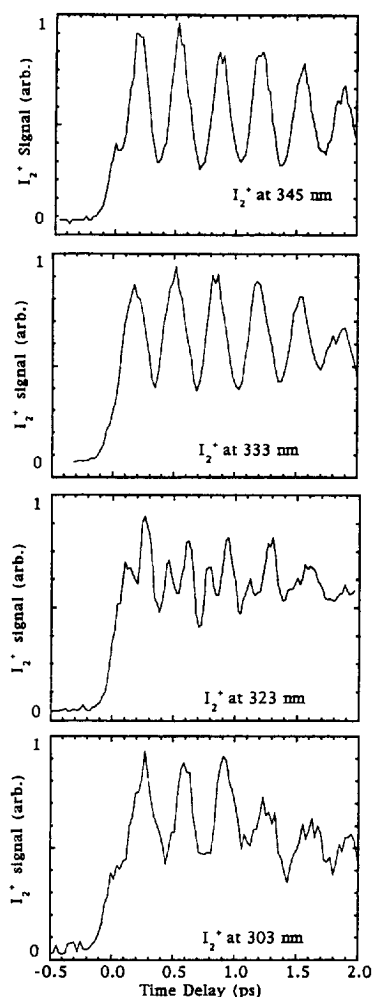


Fig. 9. Time delay scans of the molecular ion signal, I_2^+ , recorded at probe wavelengths (from top to bottom) 345, 333, 323 and 303 nm. Note that the B-state wavepacket prepared by the 580 nm pump pulse is unchanged. The observed differences appear to reflect the motion of the probe Condon point as the final ion state is changed. At 323 nm, a doubling of the modulation frequency is observed, consistent with the probe Condon point being located close to the middle of the B-state well.

Franck–Condon factors), the excess energy being carried away by the photoelectron. The total ion signal is therefore a weighted integral of transitions to all open channels. In a ZEKE scan, on the other hand, transitions are forced to terminate in final ionic states which are within the bandwidth of the probe pulse. This can lead to different effective Condon points for the ion versus ZEKE detection schemes

and therefore to different pump–probe patterns. Interestingly, the ZEKE and ion scans as well as their corresponding FTs looked quite similar to each other at each wavelength. Since we observed such similarity at each wavelength, we were initially concerned that the observed ZEKE signals might originate from space-charge (plasma) effects [47]. In such a circumstance, the “ZEKE” signal would be due to kinetic electrons which are trapped by the net charge of all positive ions, rather than a single Coulomb centre. A pulsed electric field would also extract these electrons and they would appear just as a ZEKE signal. We can, however, rule out this mechanism. If the ZEKE signal was due to plasma-trapped electrons, the signal would be present as long as ions are present in the interaction volume (the ions fly out very slowly due to their thermal velocities). However, the ZEKE signal disappeared beyond about 2 μ s, whereas the ion signals were observed (by a high voltage pulsed field ion extraction) beyond delays of 10 μ s and we can conclude that these space charge (plasma) effects do not contribute to our signal. Note that the above arguments also rule out the possibility of charge exchange between high- n Rydberg states and the surrounding I^+ ions [48]. Furthermore, as discussed below, there were some probe wavelengths where the I_2^+ and I^+ signals had different modulation patterns. The ZEKE signal always looked like the I_2^+ signal, again suggesting that plasma effects were not present.

One explanation for the similarity of the ion and ZEKE scans could be that the $X^+ \leftarrow B$ Franck–Condon factors (FCFs) continuously increase with probe photon energy, due to the extended nature of the B state. In such a case, the ion scans would be dominated by transitions to the highest available ionic levels, namely those within the laser bandwidth. Indeed, we did observe such increases in signal magnitudes as the photon energy was increased from threshold. The calculated FCFs do increase above threshold, but only up to around $v^+ = 7$ –10 for the B-state levels in our wavepacket. Beyond this region, the FCFs decrease slightly and oscillate about an average value. Therefore, it seems unlikely that we can rely upon FCFs alone to explain the observed similarity of the ion and ZEKE scans in these I_2 experiments.

One possibility is that the beating patterns are not

determined by overlaps with the ionic state but rather by an intermediate state accessed via accidental one-photon resonance. Indeed, the E and f charge transfer states of I_2 are well known to absorb strongly from the B state [49]. In such a case, as the probe laser is tuned, we would access different E,f-state vibrational levels which would determine the Condon points for detection. One-photon ionization from these states might conceivably produce similar ion and ZEKE scans. However, we can easily rule out this pathway, at least when the probe laser is tuned to the lower vibrational levels of the ionic ground state ($v^+ < 8$ –10). This is because the E and f states are greatly extended and have essentially zero Franck–Condon overlap with the lowest vibrational states of the ion: it is not possible to form $I_2^+(v = 0)$ from the E and f states. It is possible, however, that the signals from higher vibrational states of the ion do contain contributions from this (1 + 1) resonant ionization pathway. As discussed below, we would need to explain both the forms (i.e. single or double peaks) of the observed modulation patterns and their relative phase shifts (i.e. offsets from $\Delta t = 0$) as a function of wavelength in terms of the two transitions $E,f \leftarrow B$, followed by $X^+ \leftarrow E,f$. This is problematic because the Condon point for the first step tends to be closer to the B state outer turning point whereas the Condon point for the second step is at the inner turning point of the E,f states. As both transitions must occur *during* the 100 fs pulse duration of the probe laser, such a mechanism requires the wavepacket to move, on the E,f states, from one Condon point to the next before the pulse turns off. (The ion-pair states are very extended: the average vibrational period in the E and f states for this level of excitation is about 375 fs.)

Another mechanism producing similar ion and ZEKE scans as a function of wavelength could be non-Condon effects in the photoionization dynamics itself – i.e. we excite autoionizing states within our broad laser bandwidth. Autoionizing states are bound states above the ionization threshold which are coupled to the continuum [50] and excitation to these states can lead to non-Condon effects in the vibrational state distribution of the ion. For example, such coupling effects are responsible for transitions into the Franck–Condon gap observed in threshold photoelectron spectroscopy [51]. In ZEKE spectroscopy,

such effects are also well known (although in this case it is not strictly autoionization, but rather coupling of different Rydberg series). Rotational autoionization has been studied in detail in high resolution ZEKE spectroscopy [52]. In general, rotational autoionization effects are much more common than vibrational ones (non-Condon effects), due to the larger energy gap for the latter. Electronic autoionization can occur when there are low lying electronically excited states in the ion, and spin-orbit autoionization can especially be observed in molecules containing heavier atoms.

There does not appear to be a consensus as to the general importance of non-Condon effects in ZEKE spectroscopy. For example, in recent ZEKE experiments on Ag_2 , certain vibrational bands in the ion were observed with considerable intensity which should be only excited weakly within a Franck-Condon picture [53]. By contrast, ZEKE spectroscopy on the complex cluster Nb_3O is completely described within the Franck-Condon approximation [54]. Amongst other examples which seem unaffected by autoionization are molecules such as benzene [55] and diphenylamine [56]. It appears that larger molecules exhibit greater Franck-Condon behaviour than do small molecules.

In the particular case of iodine, ion yield spectra show a large number of autoionizing resonances [57,58]. As our femtosecond lasers have a broad bandwidth, it is likely that we will excite some autoionizing states. Due to their larger cross-sections, they may dominate the transitions and diminish the efficacy of a Franck-Condon analysis. Detailed studies of threshold photoelectron [62] and ZEKE spectroscopy [59] of I_2 have shown that spin-orbit autoionization from Rydberg states converging on the upper spin-orbit state of the ion lead to the observation of non-Condon effects in transitions to the ground ionic state.

Recently, in a study relevant to the present one, high resolution (nanosecond) ZEKE spectra have been recorded via two-photon ionization from $\text{I}_2(\text{B}, \nu = 15)$ valence state [60]. Evidence for autoionization was obtained. The lower vibrational levels ($\nu^+ = 0-5$) of the $\text{I}_2^+(^2\Pi_{3/2})$ ground state are essentially unperturbed by autoionization and are well described by FCFs from the B state. For the higher vibrational levels, the extent of the progression could be well

simulated by FCFs but the detailed distribution of peak intensities and the spin-orbit branching ratio reflected both spin-orbit autoionization and field induced resonant ionization. In our femtosecond experiments we simultaneously photoionize a broad range of B-state levels (approximately $\nu = 13-18$) and, for probe wavelengths beyond threshold, this projects them onto a broad range of final ionic vibrational states. This large degree of averaging may tend to wash out some sharp non-Condon features, as compared with the nanosecond experiments.

This same nanosecond study of $\text{I}_2(\text{B})$ photoionization also showed evidence of “false” ZEKE signals for $\nu^+ > 6$ (due to the trapping of kinetic electrons by plasma effects [47]) when the probe laser was tuned to certain E,f-state vibrational levels, forming large amounts of I^+ (note that I_2^+ is not formed until high vibrational levels of the ion are reached due to extremely poor FCFs with the E,f states). The likely channel for the I^+ in the nanosecond study is single-photon dissociation of the charge transfer states forming $\text{I}^+ + \text{I}^-$. These reported “false” ZEKE signals do not appear close to threshold. In fact, as can be seen in Figs. 6 and 8, our I^+ and I_2^+ signals are almost identical and hence this I^+ signal arises from dissociation of the I_2^+ ion and not from another pathway (which would give a different modulation pattern). Furthermore, in our femtosecond experiments although the intensities are relatively high, the pulse energies are very low and actually very few ions (10–100) are produced each laser shot, making trapping of free electrons unlikely. Finally, at some probe wavelengths (e.g. 323 nm), the I^+ and I_2^+ modulation patterns were indeed different, indicating different pathways, but the ZEKE signal always looked like the I_2^+ signal.

In sum, we expect that the effects of intermediate state resonances and autoionization to be absent at the ionization threshold but to contribute for higher final vibrational states of the ion. Such effects might be partially diminished as compared with the analogous nanosecond experiments due to the averaging of many initial and final states.

3.2.1. Probe wavelength dependence: modulations and phase shifts

It is interesting to consider the effect of the final state on the detection of the wavepacket dynamics.

By changing the final state, keeping the preparation step unchanged, very different modulation patterns were observed (Fig. 9). This illustrates how, in detection, the same wavepacket may appear quite different depending upon the nature of the final state. For reasons discussed in the previous section and for reasons of simplicity, we will adopt the Franck–Condon picture of the photoionization process. As will be seen, the general features of the scans and their relative variation with probe wavelength can be surprisingly well described by non-resonant two-photon ionization of the B state within the Franck–Condon approximation.

The probe Condon point is the point of best overlap of the states comprising the wavepacket with a given final state of the ion. As the probe wavelength is tuned to higher photon energies, higher vibrational levels in the ion are accessed. These will have different overlaps and hence different Condon points. We expect, therefore, that the form of the pump–probe modulation pattern will change upon changing the probe wavelength. Indeed, the scans at the different probe wavelengths shown in Fig. 9 exhibit significant differences. Most dramatically, at 323 nm probe wavelength the modulation pattern has split into sets of two peaks.

Two-photon probe excitation at 345 nm corresponds to a transition into the lowest vibrational levels $v^+ = 0, 1$ of the ionic ground state, $^2\Pi_{3/2}$. At $\lambda_{\text{pr}} = 333$ nm, the probe step will terminate around $v^+ = 10$ in the ion. Excitation at 323 nm will terminate in the vibrational levels around $v^+ = 19$. A probe wavelength of 303 nm corresponds to excitation of predominately $v^+ = 13, 14$ in the spin–orbit excited $^2\Pi_{1/2}$ state of the ion and perhaps some very high-lying v^+ levels in the lower spin–orbit state as well. The adiabatic ionization potential of the upper spin–orbit state corresponds to a probe wavelength around 318 nm [60].

For an ionic final state around $v^+ = 19$ (323 nm probe), we expect the probe Condon point to move away from the inner turning point because the B state is quite extended. This is seen in the diabatic dressed states picture for 323 nm probing, shown in Fig. 10. The probe Condon point (the intersection of the B and X^+ curves) has moved closer to the middle of the B state well and the wavepacket passes it twice upon each vibration. This accounts for the

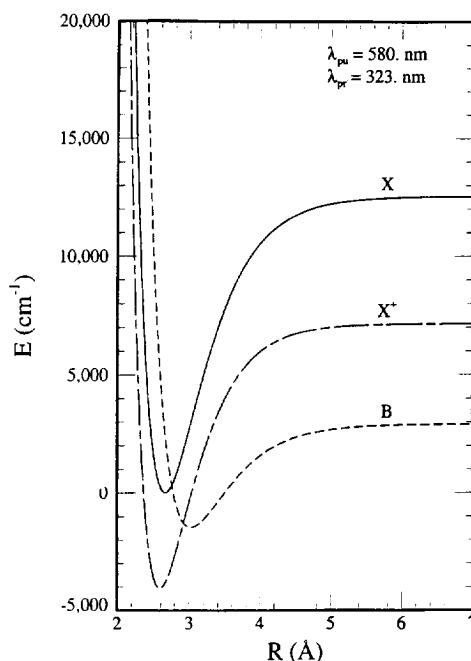


Fig. 10. Diabatic dressed states picture of I_2 photoionization at 323 nm probe wavelength. The zero in energy is defined by the ground state of the neutral, X. The B state is shifted down in energy by one pump photon, the ionic ground state, X^+ , by one pump and two probe photons. The probe Condon point, where the B and X^+ curves cross, appears close to the middle of the B state well and leads to a doublet modulation pattern.

observed doubling of the modulation frequency. A similar type of doubling in the modulation patterns of $I_2(B)$ wavepackets was previously shown in theoretical calculations [26]. The exact location of the probe Condon point determines the ratio of fundamental (340 fs) to second harmonic (170 fs) modulations seen in the scans. In Fig. 11, we show the FTs of 10 ps time delay scans for the molecular ion (top) and ZEKE (bottom) signals, recorded consecutively under identical conditions with 323 nm probe wavelength. Note that the shorter scan length (10 ps) leads to a reduction in spectral resolution and, hence, we were not able to assign these peaks. A 25 ps ZEKE time delay scan at this wavelength was presented in our previous communication [22]. The fundamental frequencies (called ω) in the FT are seen to be close to 100 cm^{-1} , corresponding to the nearest-neighbour level spacing. The second harmonic frequencies (called 2ω) around 200 cm^{-1} appear in the FT with

considerable amplitude and corresponds to next-nearest-neighbour coherences. The very strong 2ω component is related to the splitting of the peaks seen in Fig. 9 for 323 nm probe and obscures the “forbidden” 2ω components due to ion–Rydberg interactions. Note that the ion and ZEKE spectra appear quite similar, as discussed in the previous section.

The appearance of the modulation patterns is associated with changes in the location of the Condon point. It should be possible, therefore, to observe changes in the phase shift – i.e. the time offset from $\Delta t = 0$ for the appearance of the first peak. This is because the initially prepared wavepacket must now travel some distance before it achieves the favourable geometry for ionization at the probe Condon point. A method developed for accurately and precisely measuring phase shifts from a simultaneously measured non-resonant cross-correlation signal is described in Appendix B. We present, in Fig. 12, the observed

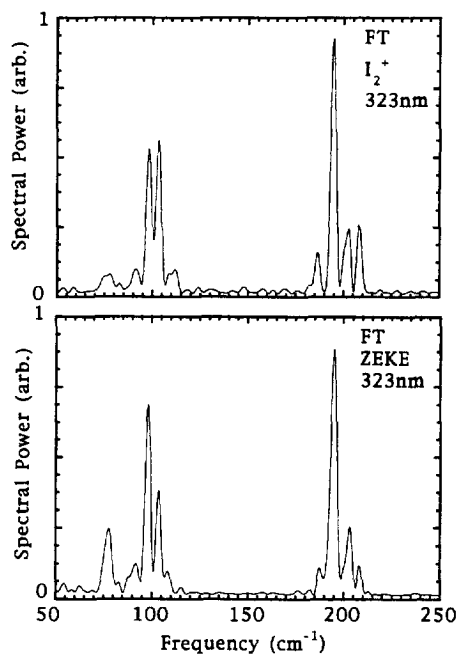


Fig. 11. Fourier transform power spectrum of 10 ps scans at $\lambda_{\text{pr}} = 323$ nm for I_2^+ (top) and the ZEKE signal (bottom). The contributions to the second harmonic are much stronger than at 345 nm (Fig. 8) due to the doublet pattern shown in Fig. 9. The ion and ZEKE spectra are quite similar. Due to the shorter scan length, the spectral resolution is reduced.

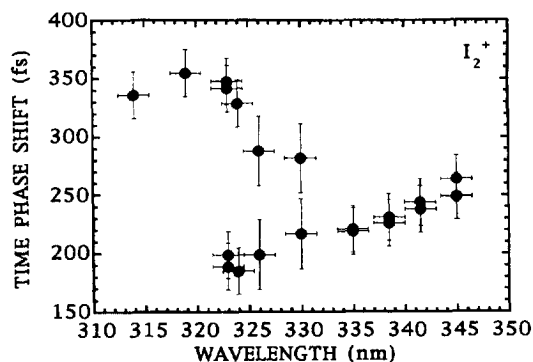


Fig. 12. Absolute phase shifts (time offset from $\Delta t = 0$, in fs) of the ion signal as a function of probe wavelength determined using the method of Appendix B. Around 330–335 nm, the peaks begin to split, reaching the full doublet structure by around 325 nm, consistent with the motion of the probe Condon point. Around 318 nm and below, the spin–orbit excited state of I_2^+ is expected to interfere.

phase shifts at several probe wavelengths, showing a systematic variation with wavelength. It can be seen that the phase shift at 345 nm was 260 ± 20 fs. This result is surprising because the ionic and neutral ground states have very similar geometries and, therefore, detection should take place from the same point where the B-state wavepacket is created, leading to a phase shift of zero. Likewise, the phase shifts at 323 nm in Fig. 12 were 190 ± 20 fs for the small peaks and 340 ± 20 fs for the large peaks (i.e. 150 fs spacing). Again, this is surprising because we expected the phase shift to increase: the probe Condon point should move to larger internuclear separations as the probe frequency is increased. Instead, the first peak at 323 nm occurred 70 fs *before* the first peak at 345 nm. This feature represents one of the most intriguing and as yet unexplained observations of our study. We are forced to conclude that the wavepacket is inefficiently prepared and/or detected when the lasers are overlapped in time. In other words, the first peak in the scans is “missing”. Although time delay scans at lower intensity did not reveal any change in the phase shift, it is possible that strong field effects such as Rabi oscillation can distort the initially prepared wavepacket. (A peak at $\Delta t = 0$, however, was observed to grow in at higher intensities but this peak was incommensurate with the rest of the modulation pattern). It is interesting to

note, in contrast with I_2 , that in similar experiments on Br_2 a large signal was observed at zero time delay [66].

In order to analyze the data in Fig. 12, we separate our discussion in two parts: (1) the relative variation of the phase shift as a function of probe wavelength; (2) the absolute phase shifts. The relative variation as a function of probe wavelength is consistent with the Condon picture used so far. We consider an increase in the probe photon energy from threshold (345 nm). The probe Condon point moves away from the inner turning point and, with the first peak missing, we detect the wavepacket for the first time when it is moving back towards the inner turning point. This leads to a smaller phase shift than at 345 nm. Furthermore, the peaks split because we detect the wavepacket twice as it passes the Condon point, going in and out, leading to the two branches observed in Fig. 12. Between 330–345 nm the splitting is small and it is difficult to determine the phase shifts accurately. Hence, the error bars are larger here. As the probe photon energy is increased further, the Condon point moves towards the middle of the well and the splitting increases, as seen in the range 320–330 nm. Below 320 nm, we observed that the small first peak disappeared and only the second peak remained. We note again that at around 318 nm, the spin–orbit excited $^2\Pi_{1/2}$ state of the ion becomes energetically accessible, which complicates the analysis.

The absolute values of the phase shifts indicate another as yet unexplained phenomenon. The phase shift of 260 fs at 345 nm does not correspond to the full vibrational period (340 fs). However, the single peak modulation pattern suggests that there is a single Condon point and that it is close to a turning point. It seems therefore that there is a time offset Δ for the wavepacket. With reference to Fig. 13, both the absolute phase shifts and the form of the modulation patterns as a function of wavelength can be reproduced if we assume that, at the peak of the pump pulse, the wavepacket had an offset of $\Delta = +80 \pm 10$ fs. We first discuss the 345 nm cartoon (Fig. 13, bottom). As discussed above, we assume that the wavepacket is not ionized efficiently during the preparation pulse. If the wavepacket is offset $+80 \pm 10$ fs, it requires an additional 90 fs to reach the other turning point. From there it takes another

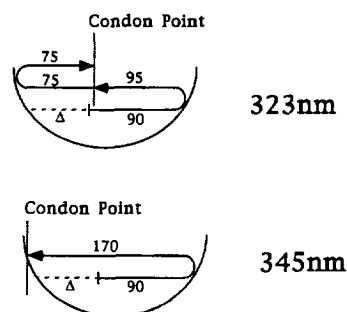


Fig. 13. Cartoon of wavepacket motion in I_2 B state for 345 nm probe (bottom) and 323 nm probe (top). The Condon points at each probe wavelength are indicated. With a single offset value of $\Delta = 80 \pm 10$ fs, the experimental phase shifts and modulation pattern are reproduced. For a discussion, see the text.

170 fs to reach the inner turning point where it is ionized for the first time at the Condon point. This is in agreement with the phase shift of 260 fs seen in Fig. 12. Furthermore, because the ionization takes place at the inner turning point, the wavepacket passes the Condon point only once upon each vibration and hence only the fundamental period of 340 fs is observed at short times, in agreement with the data in Fig. 9.

Next we consider the 323 nm cartoon in Fig. 13, top. As above, the wavepacket is offset about 80 ± 10 fs during the preparation pulse, but is not detected at the probe Condon point due to the overlap of the lasers. It then requires another 90 fs to reach the outer turning point. Since the probe Condon point is now much closer to the middle of the well, it requires only an additional 95 fs before ionization can occur for the first time. This is a phase shift of 185 fs for the first peak, in agreement with that shown in Fig. 12. The wavepacket then takes another 75 fs to reach the inner turning point and another 75 fs to return to the probe Condon point where it is ionized to give the second peak, this time heading towards the right. This corresponds to a doublet modulation pattern with 150 fs between the peaks, in agreement with observation (Fig. 9). Furthermore, a phase shift of 340 fs is obtained for the second peak, in agreement with that in Fig. 12.

It is important to note that the ad hoc offset Δ of 80 fs cannot correspond simply to wavepacket motion during the preparation pulse because the phase shifts are measured from the *peak* of the pump pulse

and its duration is less than 100 fs. Strong field effects may alter the initial phases of the wavepacket in a manner that leads to the observation of such offsets. We speculate that the “missing” peak at zero delay and the offset Δ are in fact related to each other. The “missing” peak at zero delay in the 345 nm data suggests that the pump does not produce a wavepacket at the inner turning point, but rather displaced from it, consistent with an offset of Δ .

At the shorter probe wavelengths, there may also be effects due to the E,f-state resonances. It is conceivable that while there is only one photoionization pathway at threshold, there may be two at higher photon energies. In fact, there may be slight evidence for this in the probe laser power studies, discussed in a later section. Detailed wavepacket calculations including intermediate states and possible strong field effects will be required to fully analyze this question.

3.3. Spectrograms and fractional revivals

A simple yet instructive way to display femtosecond pump–probe data on wavepacket evolution is to use a time-windowed Fourier transform power spectrum (called a spectrogram). In this method, a window function $g(t)$ of width t_0 (chosen to be 1 ps) is convoluted with a normalized time delay scan $s(t)$ and the Fourier transform power spectrum is calculated. The spectrogram is obtained by translating this window along $s(t)$, yielding a two-dimensional map of frequency content versus time delay, with the Fourier spectral power as the intensity. We define the spectrogram, $S(\omega, \tau)$ and the window, $g(t)$ in the equations below.

$$S(\omega, \tau) = \int_0^\infty s(t) g(t - \tau) e^{i\omega t} dt, \quad (4)$$

$$g(t) = e^{-t^2/t_0^2}. \quad (5)$$

Typically, we plot $\ln|S(\omega, \tau)|^2$ as a contour map in ω and τ . This is done in Fig. 14 for the 345 nm I_2^+ time delay scan of Fig. 6 (top). The intensity (dark) seen near 100 cm^{-1} frequencies at zero and 18 ps time delay corresponds to the initial wavepacket oscillation and its half-revival, respectively. In this data, the second harmonic frequency (which appears near 200 cm^{-1}) is weakly observed. In Fig. 15 we

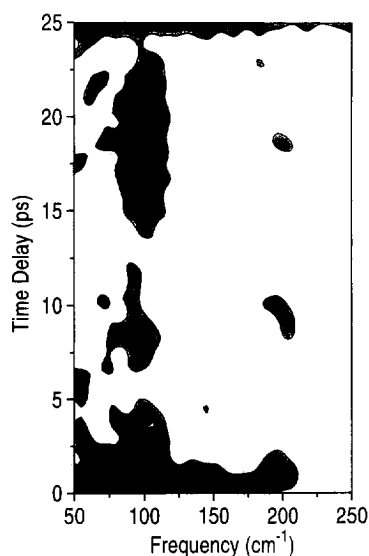


Fig. 14. Log spectrogram contour plot of the 345 nm I_2^+ scan from Fig. 6 (top), showing the spectral content of the scan as a function of time delay. The dark regions near zero and 18 ps at 100 cm^{-1} frequency correspond to the initial modulation and the half-revival seen in Fig. 6.

present the spectrogram of the 345 nm ZEKE time delay scan from Fig. 6 (bottom). As in the I_2^+ spectrogram, we see again the fundamental frequency at zero and 18 ps. We also see a strong second harmonic frequency, which appears simultaneously with the fundamental. The ion scan at 345 nm does not show this phenomenon and we can relate this to differences between ion and ZEKE detection techniques, as discussed above. Note that the intensity scale for all spectrograms was kept constant, allowing a direct comparison of spectral powers at different probe wavelengths.

In Figs. 16 and 17 we present spectrograms of the I_2^+ and ZEKE scans at 323 nm probe wavelength, respectively. The fundamental vibrational frequency around 100 cm^{-1} can be seen at zero delay and around 18 ps ($T_{\text{rev}}/2$, the half-revival). The second harmonic frequency at around 200 cm^{-1} also appears at zero and 18 ps. This is expected since the second harmonic contribution at these time delays arises due to the location of the probe Condon point. Interestingly, the second harmonic also appears at a delay of 9 ps ($T_{\text{rev}}/4$) where it is *not* accompanied by any fundamental frequency intensity. This is the

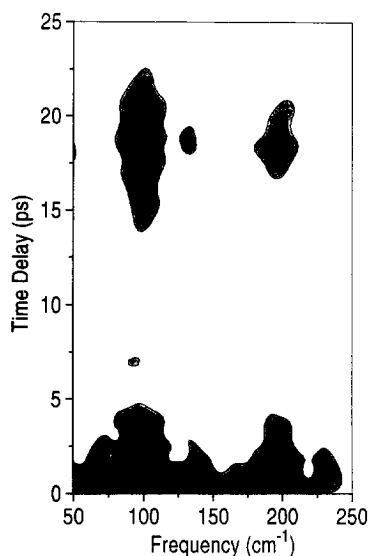


Fig. 15. Log spectrogram contour plot of the 345 nm ZEKE scan from Fig. 6 (bottom), showing the spectral content of the scan as a function of time delay. The dark regions near zero and 18 ps at 100 cm^{-1} frequency correspond to the initial modulation and the half-revival seen in Fig. 6. The strong second harmonic near 200 cm^{-1} which appears simultaneously with the fundamental frequency is not seen in the ion spectrogram (Fig. 13) and is indicative of differences between ion and ZEKE detection.

quarter-revival, where the wavepacket has split into two. (Presumably, because of the location of the Condon point at 323 nm, the splitting of the wavepacket at 9 ps would also lead to a quartet modulation pattern and therefore a fourth harmonic frequency in the FT. However, this exceeds the time resolution of our laser system).

In order to illustrate the quarter-revival, we show B-state wavepacket simulations in Fig. 18. In these simulations, the X and the B state constants from Ref. [61] were used to fit Morse parameters. For X^+ , the Morse parameters were adjusted to fit published photoelectron spectra [62] and ab initio calculations [63]. Rotations and effects due to the non-zero duration of the laser pulses were ignored, as were possible effects due to saturation. In Fig. 18, we see the reconstructed wavepacket at zero delay and 18 ps. At a random intermediate time, say 4.3 ps, the wavepacket is delocalized. At the specific time delay of 9 ps, we can see that the wavepacket has split into two equal parts exactly out of phase: this is the quarter-revival and its occurrence at this time delay

is in agreement with the data shown in the spectrograms of Figs. 16 and 17. Quarter-revivals have been previously observed in atomic Rydberg systems [43] and appearance of second harmonic frequency in an atomic FT is sufficient proof of this: there is only one “Condon point” for ionizing a Rydberg atom – at the ion core. In a molecule, however, there are several mechanisms for producing the second harmonic frequency. Examples are: the location of the Condon point as discussed above; the possible existence of two Condon points, such as in the Na_2 system [64]; non-adiabatic predissociative coupling of potential curves, as seen in the NaI system [65] (see also Ref. [1]); and fractional revivals. The clearest proof of a fractional revival in molecular systems comes from a spectrogram showing that a harmonic occurs at regular well defined time delays concomitant with the absence of the fundamental frequency. In Figs. 16 and 17, the 200 cm^{-1} intensity seen in between the quarter revival and the half-revival (and $\Delta t = 0$) are due to higher-order rephasings of the wavepacket. An experimental study (including obser-

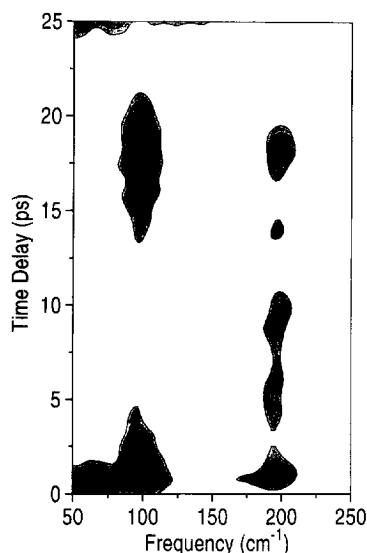


Fig. 16. Log spectrogram contour plot of a 25 ps I_2^+ scan at 323 nm probe wavelength, showing the spectral content of the scan as a function of time delay. The dark regions near zero and 18 ps at 100 cm^{-1} frequency correspond to the initial modulation and the half-revival. The second harmonic near 200 cm^{-1} which appears simultaneously with the fundamental frequency is expected for this location of the Condon point. Evidence of higher-order fractional revivals is seen.

vation of the third harmonic) and detailed discussion of fractional revivals in an anharmonic molecular potential (Br_2) is reported elsewhere [66].

3.4. Intensity dependence

An advantage of the high peak intensities in femtosecond experiments lies in the possible application of multiphoton excitation and detection schemes. With such schemes it was possible to study the wavepacket dynamics in the ion-pair states of I_2 [72]. Intensity effects were studied recently in NaI [67]. However, high laser intensity can also affect spectroscopic observations and even the molecular dynamics itself [68]. In recent experiments on Na_2 [69], for example, a strong coupling between the electronic ground and first excited states was induced by the pump step, leading to the observation of ground state wavepacket motion. Intense fields were observed to strongly modify potential energy surfaces in HCl^+ in the long wavelength limit [70] and in H_2^+ at optical frequencies [71]. Another study

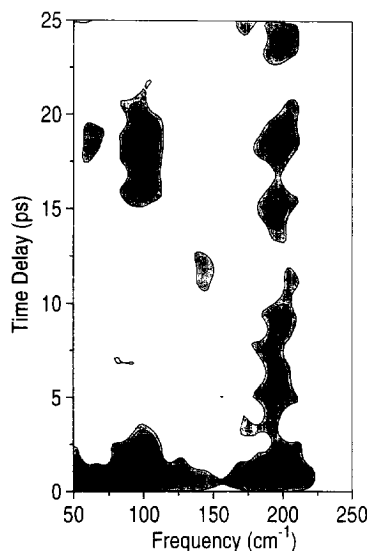


Fig. 17. Log spectrogram contour plot of a 25 ps ZEKE scan at 323 nm probe wavelength, showing the spectral content of the scan as a function of time delay. The dark regions near zero and 18 ps at 100 cm^{-1} frequency correspond to the initial modulation and the half-revival. As in the ion scan, the second harmonic near 200 cm^{-1} which appears simultaneously with the fundamental frequency is expected for this location of the Condon point. Evidence of higher-order fractional revivals is seen.

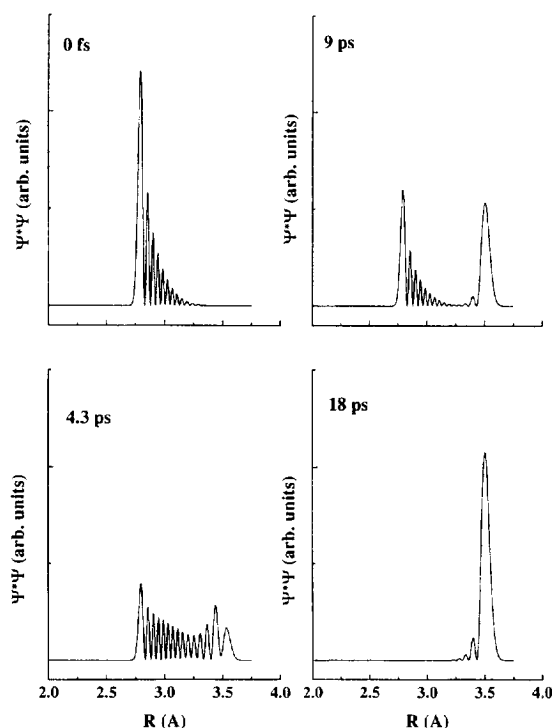


Fig. 18. Wavepacket calculation for the iodine B state. The wavepacket is created at the inner turning point (top left). Due to the anharmonicity of the vibrational B-state levels it dephases (bottom left) and has always some amplitude at the probe Condon point. The quarter-revival is seen at 9 ps (top right), where the wavepacket has split into two equal parts exactly out of phase. At 18 ps (bottom left) is the half-revival. It can be seen that the wavepacket at 9 ps appears as the normalized sum of the wavepackets at zero and 18 ps. Rotational and pulse duration effects are neglected.

investigated ponderomotive effects in ZEKE photoelectron spectroscopy when using intense femtosecond pulses [18]. Therefore, at three probe wavelengths, $\lambda_{\text{pr}} = 345, 323$ and 303 nm , we studied the laser intensity dependence of the signal (at short delay times). The laser intensities were varied by over one order of magnitude. It was found that the pump laser intensity had only a small effect on the modulation depths and no observable effect on the phase shifts. The probe laser intensity dependence, on the other hand, did show an effect. For both $\lambda_{\text{pr}} = 345$ and 303 nm , the modulation pattern did not change with intensity. It did change significantly at $\lambda_{\text{pr}} = 323\text{ nm}$, as shown in Fig. 19. At “full” probe laser intensity, about $I_0 = 1 \times 10^{12}\text{ W/cm}^2$

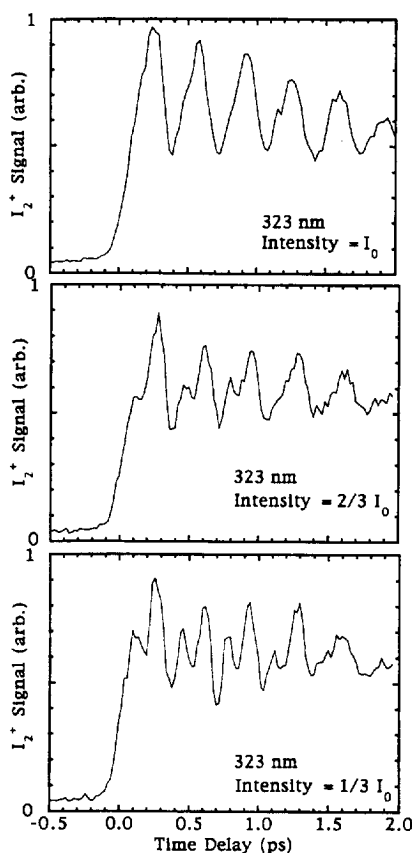


Fig. 19. Ion signal time delay scans at a probe wavelength of 323 nm, recorded at different probe laser intensities: I_0 (top trace), $2/3I_0$ (middle trace) and $1/3I_0$ (bottom trace). The well resolved doublet modulation pattern appears upon reduction of the probe laser intensity.

(top trace) only a single modulation with a 340 fs period is visible, although a slight asymmetry on the left side of the peaks is visible. When the laser intensity is reduced to about $2/3$ of this value, the second series of smaller peaks grows in (middle trace). This is clearest when the intensity is reduced to $1/3$ of I_0 . (At still lower intensities, the signal-to-noise ratio degraded.) It perhaps seems that the second peak grows at the expense of the first as the laser power is increased. If this is correct, it may indicate two distinct ionization pathways. However, these results may simply be due to saturation effects: In a data ensemble of single-shot signals as a function of probe laser energy, we could observe saturation effects at higher pulse energies.

4. Conclusion

In the present experiments we probed the wavepacket dynamics in the B state of iodine by detecting either ZEKE electrons or ions in a $[1 + 2]$ multiphoton process. A detailed description of the synchronized fs/ps laser system and the molecular beam photoelectron/photoion spectrometer was presented. With probe excitation tuned to the ionization threshold, wavepacket motion with an average vibrational period of 340 fs was observed, as well as the dephasing and half-revival of the wavepacket. Fourier transform power spectra (FTs) of the time delay scans revealed that the observed frequencies are due to level spacings in the B state. A threshold tuning curve demonstrated that the signal is due to a one-photon preparation and two-photon ionization of the B state. The ZEKE scans exhibited deeper modulation depths than the ion scans. Furthermore, some new frequencies were observed in the ZEKE scans (at the second harmonic) which do not correspond to level spacings in the B state. Both these effects were related to aspects of the ZEKE detection technique itself (specifically, ion–Rydberg interactions).

In order to further explore differences between ion and ZEKE detection, we varied the probe wavelength from threshold to above the onset of the spin–orbit excited ion state. Generally, the appearance of ZEKE and ion scans and their FTs was quite similar as a function of probe wavelength. This may be related to intermediate state resonances and to possible non-Condon effects due to autoionization. It was observed that the form of the modulation pattern changes with probe wavelength and that these variations could be understood within the Franck–Condon picture. For example, at 323 nm, a doubling of the modulation frequency was observed. This was related to the motion of the Condon point with probe wavelength. At 323 nm, the Condon point is expected to be close to the middle of the B state well and, therefore, the wavepacket must pass it twice upon each oscillation.

The relative form and phase shifts (offset from $\Delta t = 0$) of the modulation patterns as a function of probe wavelength suggested that the ionization process can be generally understood with a Franck–Condon picture. However, one of the most interesting (unexplained) aspects of these experiments is the

absence of a peak at zero delay with 345 nm detection. This indicates that a “proper” wavepacket is somehow not efficiently prepared or detected when the lasers are overlapped in time, perhaps due to strong field effects. The absolute phase shifts indicate that there is an offset Δ of the wavepacket during the pump pulse. A single value of $\Delta = 80 \pm 10$ fs allowed us to self-consistently reproduce the variation of *both* (1) the form and (2) the absolute phase shifts of the modulation patterns with probe wavelength, using the Condon picture. It is noteworthy that the offset Δ is too large to be simply due to wavepacket motion during the preparation pulse and this may also indicate strong field effects.

Time-windowed Fourier transform power spectra (spectrograms) were introduced to reveal the frequency content of the scans as a function of time delay. Evidence of higher-order fractional revivals was seen in the spectrograms and supported by wavepacket calculations. Intensity effects due to the probe laser, obscuring high frequency modulations, were observed.

Acknowledgements

We acknowledge stimulating discussions with T. Seideman, I. Averbukh, P.B. Corkum, M.Yu. Ivanov and M. Shapiro. We are indebted to B. Avery, D. Roth and D. Joines for expert technical assistance, as well as the NRC Mechanical and Optical Components Laboratories. We thank P. Dooley (NRC Summer Research Assistant) for developing much of the data acquisition routines.

Appendix A. Ionization threshold tuning curves

In this Appendix, we discuss and rule out the possibility that the observed pump–probe signals do not originate from single-photon preparation and two-photon detection of the B state. Femtosecond pump–probe experiments are often high intensity experiments. The absorption of multiple pump photons is possible [72]. Two pump photons can excite iodine into the directly dissociative 0_g^+ and three photons into the $D0_u^+$ (the lowest lying ion-pair state). In the D state, the wavepacket oscillates with

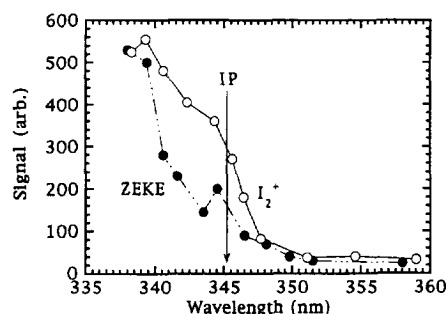


Fig. 20. Threshold probe wavelength tuning curve for molecular ion (full line) and ZEKE electrons (dashed line) detection. Both curves show the correct onset of the signal at the ionization potential (IP), indicating single-photon preparation and two-photon detection of the B-state wavepacket.

a different vibrational period (corresponding to a vibrational level spacing of $\Delta G_v < 90 \text{ cm}^{-1}$ in the region of the D state that would be excited by three photons [73]). In our experiments it must be confirmed that a $[1+2]$ process was detected, as opposed to some competing higher-order process. As the FTs revealed only the known structure of the B state, higher-order pump processes were not detected. However, it might have been possible to ionize the B state with a highly multiphoton probe process. Were this true, the probe laser could be tuned below the two-photon threshold for ionization and signals still recorded. The threshold probe laser tuning curves were measured for both ZEKE electrons and molecular ions, shown in Fig. 20. As we tuned our probe laser, the pulse duration and bandwidth remained constant, but there was a small shift in the $\Delta t = 0$ point due to the slightly different paths through the colour-picker. In order to avoid recalibration of $\Delta t = 0$ for each wavelength, the tuning curves were recorded at long delay times (30 ps), where no modulations were present in the time delay scan. Both curves shown reveal the onset of the signal around the ionization potential (345 nm), proving that the probe signal is indeed due to two-photon excitation into the lowest vibronic levels of the ion. (Note that the broad bandwidth of femtosecond pulses prevents a sharp determination of the ionization potential.) The absorption of three probe photons would terminate in the B^+ state of I_2^+ . Such a process should set in far more to the red (i.e. below

the IP). Thus, any significant contribution from this process can be excluded from the tuning curves of both ion and ZEKE signals. Furthermore, the B^+ state is predissociative [74] and should not yield a molecular ion signal. However, we were able to record a time delay scan below the two-photon threshold (not shown). As can be seen from Fig. 20, the signal levels for such a scan are much lower. We obtained a noisy pattern which was very different from the one obtained above threshold and is probably due to the probing of higher-order pump processes.

Appendix B. Determination of $\Delta t = 0$ and the phase shift

An accurate determination of the zero delay time, that is when pump and probe pulses are temporally overlapped at the molecular beam, is essential in order to determine the absolute phase shifts and therefore the relative locations of the Condon points for the pump and probe processes. We routinely recorded the cross-correlation (CC) of the pump and probe lasers, after they left the vacuum chamber, by sum-frequency mixing in a 0.1 mm β -BBO crystal. The $\Delta t = 0$ determined in this way was shifted from the $\Delta t = 0$ at the molecular beam axis because of the group velocity dispersion (GVD) between the two pulses in the thin exit window of the vacuum chamber. In order to correct for this, an identical thin window was put in the beam path before the CC crystal in order to measure a window delay of 125 ± 10 fs at 333 nm probe wavelength. This allowed for convenient simultaneous recording of the CC during the iodine scans, as shown in Fig. 21. An ideal method to check the $\Delta t = 0$ calibration is to record a two-laser non-resonant ionization signal at the molecular beam. In our case, it was convenient to use Xe(g). Both the BBO sum-frequency mixing (using the 125 ± 10 fs window correction) and the Xe non-resonant ionization methods gave the same zero in time (to within 10 fs) and therefore we are confident of the CC data obtained using the window-corrected sum-frequency mixing signal and used it at all probe wavelengths reported. The correction required for the change in GVD over the 300–350 nm range of probe wavelengths we estimate to

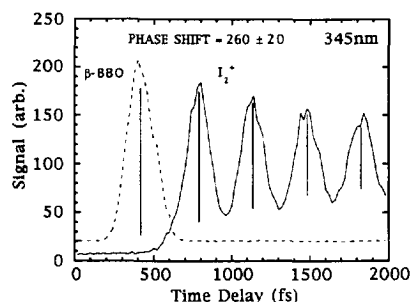


Fig. 21. An accurate determination of the zero in time is accomplished by simultaneously recording a sum-frequency mixing signal (β -BBO) and the signal of molecular iodine at 345 nm. The BBO signal was corrected for GVD in the exit window and centroids of the ion peaks were fit to a straight line and extrapolated to zero in order to obtain a phase shift of 260 ± 20 fs. The precision of the method was confirmed by measuring a non-resonant signal from Xe(g).

be small (about ± 20 fs). (It is interesting to note that “non-resonant” ionization of NO(g) gave a wavelength-dependent 30–50 fs error in the determination of $\Delta t = 0$; care must be taken to strictly avoid resonances when determining the absolute zero of time. Due to their higher density of states, we might expect molecular signals to be more problematic).

A third, independent, method was used to check the correct assignment of $\Delta t = 0$. This method is based upon an analysis of the separate sine and cosine Fourier transforms of the measured time delay scans: at the correct $\Delta t = 0$, as can be seen from Eq. (3), the imaginary component (sine) must be minimized for all frequencies. Therefore, this technique replaces t by $(t - t_0)$ in the measured delay scans and varies t_0 such that the imaginary Fourier component is minimized for all frequencies. This yields a set of “candidate” times for $\Delta t = 0$ with an accuracy of ± 10 fs, each separated by one-half an average vibrational period (about 170 fs). The maximization of the real (cosine) component can be used as a check of the assignment. The experimentally determined $\Delta t = 0$ is then compared with the closest “candidate” time. The agreement was generally good (± 20 fs).

We now consider the determination of the phase shift of the I_2 modulation pattern at 345 nm probe. The solid vertical lines shown in Fig. 21 represent the centroids of the peaks. As discussed above, the

zero of time was determined to be 125 ± 10 fs to the right of the CC trace centroid in Fig. 21. The centroids of the ion peaks were least-squares fit to a straight line and extrapolated to zero in order to determine the phase shift (i.e. the position of the first peak with respect to the zero of time) of the modulation pattern. This reproducibly determined the phase shift to be 260 ± 20 fs for the probe wavelength of 345 nm. The phase shifts at the other probe wavelengths shown in Fig. 12 were determined in a similar manner.

References

- [1] A.H. Zewail, Faraday Discussions Chem. Soc. 91 (1991) 207; Femtosecond chemistry (World Scientific, Singapore, 1994).
- [2] E.J. Heller, Accounts Chem. Res. 14 (1981) 368.
- [3] T.S. Rose, M.J. Rosker and A.H. Zewail, J. Chem. Phys. 88 (1988) 6672.
- [4] S.I. Ionov, G.A. Brucker, C. Jaques, L. Valachovic and C. Wittig, J. Chem. Phys. 99 (1993) 6553.
- [5] J.H. Glowia, J. Misewich and P.P. Sorokin, in: The supercontinuum laser source, ed. R.R. Alfano (Springer, Berlin, 1990).
- [6] Y. Chen, L. Hunziker, P. Ludowise and M. Morgen, J. Chem. Phys. 97 (1992) 2149.
- [7] T. Baumert, M. Grosser, R. Thalweiser and G. Gerber, Phys. Rev. Letters 67 (1991) 3753.
- [8] M. Dantus, M.H.M. Janssen and A.H. Zewail, Chem. Phys. Letters 181 (1991) 281.
- [9] P.M. Felker and A.H. Zewail, Phys. Rev. Letters 53 (1984) 501.
- [10] V. Engel, Chem. Phys. Letters 178 (1991) 130; Ch. Meier and V. Engel, Chem. Phys. Letters 212 (1993) 691; J. Chem. Phys. 101, 2673 (1994); Phys. Rev. Letters 73 (1994) 3207.
- [11] M. Seel and W. Domcke, J. Chem. Phys. 95 (1991) 7806.
- [12] K. Müller-Dethlefs, M. Sander and E.W. Schlag, Z. Naturforsch. 39a (1984) 1089.
- [13] K. Müller-Dethlefs and E.W. Schlag, Annu. Rev. Phys. Chem. 42 (1991) 109.
- [14] H. Krause and H.J. Neusser, J. Chem. Phys. 99 (1993) 6278.
- [15] J.M. Smith, C. Lakshminarayan and J.L. Knee, J. Chem. Phys. 93 (1990) 4475.
- [16] J.M. Smith, X. Zhang and J.L. Knee, J. Chem. Phys. 99 (1993) 2550.
- [17] T. Baumert, R. Thalweiser and G. Gerber, Chem. Phys. Letters 209 (1993) 29.
- [18] A. Zavrilyev, I. Fischer, D.M. Villeneuve and A. Stolow, Chem. Phys. Letters 234 (1995) 281.
- [19] M.C.R. Cockett, H. Ozeki, K. Okuyama and K. Kimura, J. Chem. Phys. 98 (1993) 7763.
- [20] D.G. Imre, J.L. Kinsey, A. Sinha and J. Krenos, J. Phys. Chem. 88 (1984) 3956.
- [21] A. Strobel, I. Fischer, A. Lochschmidt, K. Müller-Dethlefs and V.E. Bondybey, J. Phys. Chem. 98 (1994) 2024.
- [22] I. Fischer, D.M. Villeneuve, M.J.J. Vrakking and A. Stolow, J. Chem. Phys. 102 (1995) 5566.
- [23] R.M. Bowman, M. Dantus and A.H. Zewail, Chem. Phys. Letters 161 (1989) 297.
- [24] M. Dantus, M.H.M. Janssen and A.H. Zewail, Chem. Phys. Letters 181 (1991) 281.
- [25] M. Gruebele and A.H. Zewail, J. Chem. Phys. 98 (1993) 883.
- [26] H. Metiu and V. Engel, J. Chem. Phys. 93 (1990) 5693.
- [27] C. Momma, H. Eichmann, A. Tünnermann, P. Simon, G. Marowsky and B. Wellegehausen, Opt. Letters 18 (1993) 1180.
- [28] J.H. Glowia, M. Kaschke and P.P. Sorokin, Opt. Letters 5 (1992) 337.
- [29] D.M. Villeneuve, I. Fischer and A. Stolow, Opt. Commun. 114 (1995) 141.
- [30] See, e.g.: The supercontinuum laser source, ed. R.R. Alfano (Springer, New York, 1989).
- [31] J.D. Kafka, M.L. Watts and J.-W.J. Pieterse, IEEE J. Quantum Electron. 28 (1992) 2151.
- [32] D.E. Spence, W.E. Sleat, J.M. Evans, W. Sibbett and J.D. Kafka, Opt. Commun. 101 (1993) 286.
- [33] C. Rolland and P.B. Corkum, Opt. Commun. 59 (1986) 64.
- [34] T. Sizer II, J.D. Kafka, A. Krisiloff and G. Mourou, Opt. Commun. 39 (1981) 259.
- [35] M.D. Perry, O.L. Landen, J. Weston and R. Ettelbrick, Opt. Letters 14 (1989) 42.
- [36] P. Simon, S. Szatmari and F.P. Schäfer, Opt. Letters 16 (1991) 1569.
- [37] J.H. Glowia, D.R. Gnass and P.P. Sorokin, J. Opt. Soc. Am. B 11 (1994) 2427.
- [38] P.W. Milloni and J.H. Eberly, Lasers (Wiley, New York, 1988).
- [39] D. Proch and T. Trickl, Rev. Sci. Instrum. 60 (1989) 713.
- [40] W.C. Wiley and I.H. McLaren, Rev. Sci. Instrum. 26 (1955) 1150.
- [41] J.L. Krause, M. Shapiro and R. Bersohn, J. Chem. Phys. 94 (1991) 5499.
- [42] I.Sh. Averbukh and N.F. Perel'man, Sov. Phys. Usp. 34 (1991) 572.
- [43] J.A. Yeazell and C.R. Stroud Jr., Phys. Rev. A 43 (1991) 5153.
- [44] J. Tellinghuisen, Advan. Chem. Phys. 60 (1985) 299.
- [45] J. Tellinghuisen, J. Chem. Phys. 58 (1973) 2821.
- [46] M.J.J. Vrakking, I. Fischer, D.M. Villeneuve and A. Stolow, J. Chem. Phys. 103, 4538 (1995).
- [47] D.M. Villeneuve, I. Fischer, A. Zavrilyev and A. Stolow, in preparation.
- [48] C. Alt, W.G. Scherzer, H.L. Selzle and E.W. Schlag, Chem. Phys. Letters 224 (1994) 366; C. Alt, W.G. Scherzer, H.L. Selzle, E.W. Schlag, L.Ya. Baranov and R.D. Levine, J. Phys. Chem. 99 (1995) 1660.

- [49] K.P. Lawley and R.J. Donovan, *J. Chem. Soc. Faraday Trans. 89*, 1885 (1993).
- [50] For a discussion of autoionizing resonances and their influence on photoionization and photoelectron spectra see: J. Berkowitz, *Photoabsorption, photoionization and photoelectron spectroscopy* (Academic Press, New York, 1979).
- [51] I. Nenner and J.A. Beswick, in: *Handbook on synchrotron radiation*, Vol. 2, ed G.V. Marr (Elsevier, 1987); W.A. Chupka, P.J. Miller and E.E. Eyler, *J. Chem. Phys.* 88 (1988) 3032.
- [52] F. Merkt and T.P. Softley, *Intern. Rev. Phys. Chem.* 12 (1993) 205.
- [53] G.I. Nemeth, H. Ungar, C. Yereztian, H. Selzle and E.W. Schlag, *Chem. Phys. Letters* 228 (1994) 1; C. Yereztian, R.H. Hermann, H. Ungar, H.L. Selzle, E.W. Schlag and S.H. Lin, *Chem. Phys. Letters* 239 (1995) 61.
- [54] D.-S. Yang, M.Z. Zgierski, D.M. Rayner, P.A. Hackett, A. Martinez, D.R. Salahub, P.-N. Roy and T. Carrington Jr., *J. Chem. Phys.*
- [55] I. Fischer, R. Lindner and K. Müller-Dethlefs, *J. Chem. Soc. Faraday Trans.* 90 (1994) 2425, and references therein.
- [56] M.G.H. Boogaarts, P.C. Hinnen and G. Meijer, *Chem. Phys. Letters* 223 (1994) 537.
- [57] J.A. Myer and J.A.R. Samson, *J. Chem. Phys.* 52 (1969) 716.
- [58] V.H. Dibeler, J.A. Walker, K.E. McCulloh and Henry M. Rosenstock, *Intern. J. Mass Spectrom. Ion Phys.* 7 (1971) 209.
- [59] M.C.R. Cockett, J.G. Goode, K.P. Lawley and R.J. Donovan, *J. Chem. Phys.* 102 (1995) 5226.
- [60] M.C.R. Cockett, *J. Phys. Chem.*, in press.
- [61] G. Herzberg, *Spectra of diatomic molecules* (van Nostrand, Princeton, NJ, 1950).
- [62] A.J. Yench, M.C.R. Cockett, J.G. Goode, R.J. Donovan, A. Hopkirk and G.C. King, *Chem. Phys. Letters* 229 (1994) 347.
- [63] A.D. McLean, O. Gropen and S. Huzinaga, *J. Chem. Phys.* 73 (1980) 396.
- [64] T. Baumert, B. Bühler, M. Grosser, R. Thalweiser, V. Weiss, E. Wiedenmann and G. Gerber, *J. Phys. Chem.* 95 (1991) 8103; T. Baumert, M. Grosser, R. Thalweiser and G. Gerber, *Phys. Rev. Letters* 67 (1991) 3753.
- [65] Ch. Meier, V. Engel and J.S. Briggs, *J. Chem. Phys.* 95 (1991) 7337.
- [66] M.J.J. Vrakking, D.M. Villeneuve and A. Stolow, submitted.
- [67] A. Materny, J.L. Herek, P. Cong and A.H. Zewail, *J. Phys. Chem.* 98 (1994) 3352.
- [68] See e.g.: *Molecules in laser fields*, ed. A. Bandrauk (Dekker, New York, 1994).
- [69] T. Baumert, V. Engel, C. Meier and G. Gerber, *Chem. Phys. Letters* 200 (1992) 488.
- [70] P. Dietrich and P.B. Corkum, *J. Chem. Phys.* 97 (1992) 3187.
- [71] A. Zavriyev, P.H. Bucksbaum, J. Squier and F. Salane, *Phys. Rev. Letters* 70 (1993) 1077.
- [72] R.M. Bowman, M. Dantus and A.H. Zewail, *Chem. Phys. Letters* 174 (1990) 546.
- [73] T. Ishiwata, J. Yamada and K. Obi, *J. Mol. Spectry.* 114 (1985) 60.
- [74] J.H.D. Eland, *J. Chem. Phys.* 70 (1976) 2926.